PAPER

Direct evidence for high Na⁺ mobility and high voltage structural processes in P2-Na$_x$[Li$_y$Ni$_z$Mn$_{1−y−z}$]O$_2$ (x, y, z ≤ 1) cathodes from solid-state NMR and DFT calculations†

R. J. Clément,‡[a] J. Xu,[bc] D. S. Middlemiss,[ad] J. Alvarado,[b] C. Ma,[b] Y. S. Meng[b] and C. P. Grey*[a]

Structural processes occurring upon electrochemical cycling in P2-Na$_x$[Li$_y$Ni$_z$Mn$_{1−y−z}$]O$_2$ (x, y, z ≤ 1) cathode materials are investigated using ^{23}Na and ^{7}Li solid-state nuclear magnetic resonance (ssNMR). The interpretation of the complex paramagnetic NMR data obtained for various electrochemically-cycled Na$_x$Ni$_{1/3}$Mn$_{2/3}$O$_2$ and Na$_x$Li$_{0.12}$Ni$_{0.22}$Mn$_{0.66}$O$_2$ samples is assisted by state-of-the-art hybrid Hartree–Fock/density functional theory calculations. Two Na crystallographic environments are present in P2-Na$_x$[Li$_y$Ni$_z$Mn$_{1−y−z}$]O$_2$ compounds, yet a single ^{23}Na NMR signal is observed with a shift in-between those computed for edge- and face-centered prismatic sites, indicating that Na-ion motion between sites in the P2 layers results in an average signal. This is the first time that experimental and theoretical evidence are provided for fast Na-ion motion (on the timescale of the NMR experiments) in the interlayer space in P2-type Na$_x$TMO$_2$ materials. A full assignment of the ^{7}Li NMR data confirms that Li substitution delays the P2 to O2 phase transformation taking place in Na$_x$Ni$_{1/3}$Mn$_{2/3}$O$_2$ over the range 1/3 ≥ x_{Na} ≥ 0. ^{23}Na ssNMR data demonstrate that Na$_x$Ni$_{1/3}$Mn$_{2/3}$O$_2$ samples charged to ≥3.7 V are extremely moisture sensitive once they are removed from the cell, water molecules being readily intercalated within the P2 layers leading to an additional Na signal between 400 and 250 ppm. By contrast, the lithiated material Na$_x$Li$_{0.12}$Ni$_{0.22}$Mn$_{0.66}$O$_2$ shows no sign of hydration until it is charged to ≥4.4 V. Since both TMO$_2$ layer glides and water intercalation become increasingly favorable as more vacancies are present in the Na layers, the higher stability of the Li-doped P2 phase at high voltage can be accounted for by its higher Na content at all stages of cycling.

aDepartment of Chemistry, University of Cambridge, Cambridge, CB2 1EW, UK. E-mail: cpg27@cam.ac.uk

bDepartment of NanoEngineering, University of California San Diego, La Jolla, CA 92037, USA

cDepartment of Materials Science and Engineering, Iowa State University, Ames, IA 50011, USA

dDepartment of Chemistry, University of Warwick, Coventry, CV4 7AL, UK

† Electronic supplementary information (ESI) available: High field ^{23}Na ssNMR data for P2-Na$_{2/3}$Ni$_{1/3}$Mn$_{2/3}$O$_2$; fits of ^{23}Na NMR spectra collected on electrochemically-cycled P2-Na$_x$Ni$_{1/3}$Mn$_{2/3}$O$_2$ samples; ^{1}H ssNMR and *ex situ* XRD data for a 4.4 V charged P2-Na$_x$Li$_{0.12}$Ni$_{0.22}$Mn$_{0.66}$O$_2$ sample; additional computational details for the CRYSTAL09 calculations; first principles magnetic exchange couplings and site-specific Ni and Mn scaling factors in Na$_x$[Li$_y$Ni$_z$Mn$_{1−y−z}$]O$_2$ compounds; first principles relaxation of P2-Na$_x$[Li$_y$Ni$_z$Mn$_{1−y−z}$]O$_2$ (x, y, z ≤ 1) structures and consequences on spin density transfer pathway geometries; Li shifts for O_h sites in O2 layers. See DOI: 10.1039/c6ta09601h

‡ Current address: Department of Materials Science and Engineering, University of California Berkeley, Berkeley, CA 94720, USA.

1. Introduction

Na-ion batteries (NIBs) are inexpensive and sustainable alternatives to Li-ion batteries (LIBs). In recent years, a significant research effort has been devoted to finding high performance Na electrode materials and electrolytes. In particular, a number of studies have focused on sodium transition metal oxides (Na$_x$TMO$_2$, TM = transition metal) as cathode materials due to their high volumetric capacities, yielding volumetric energy densities comparable to current commercial LIBs.[1–8] Layered oxides based on the P2 structure, in Delmas *et al.*'s nomenclature system[9] (where 'P' indicates prismatic Na, and '2', AB BA oxygen layer stacking), are promising NIB cathodes with a high Na-ion conductivity. TMO$_2$ layer glides can occur upon electrochemical Na extraction, leading to phase transitions at high voltage.[2–4,10–15] Starting from a P2 phase, layer shearing leads to the formation of O2-type layers (AB CB stacking) with Na⁺ ions in octahedral environments and reduced Na⁺ mobility.[3] Preventing this layer shearing has therefore been proposed to be important for improving

This journal is © The Royal Society of Chemistry 2017

J. Mater. Chem. A, 2017, 5, 4129–4143 | 4129

capacity retention, rate performance, and cycle life for P2-$Na_x TMO_2$ cathodes.

Previous work on the P2-$Na_{2/3}Ni_{1/3}Mn_{2/3}O_2$ cathode showed that the 2 : 1 Mn : Ni ratio leads to honeycomb ordering on the TM lattice,[3] as shown in Fig. 1. All Na^+ ions can be extracted upon first charge, leading to a high initial reversible capacity of 161 mA h g^{-1} at a cycling rate of 5 mA g^{-1}, close to the theoretical value of 173 mA h g^{-1} based on the Ni^{2+}/Ni^{4+} redox reaction.[2,3] Mn was found to be electrochemically-inactive, remaining in its tetravalent state throughout. However, the rapid performance degradation of this material has motivated several groups to investigate low levels of Ni substitution by an electrochemically inactive species, such as Mg[16,17] or Li,[18] to develop materials with improved performance. The present work builds upon a previous report on the Li-doped P2-$Na_{0.8}Li_{0.12}Ni_{0.22}Mn_{0.66}O_2$ cathode[19] and investigates the role of Li doping, comparing the structural processes taking place upon cycling in undoped P2-$Na_{2/3}Ni_{1/3}Mn_{2/3}O_2$ and Li-doped P2-$Na_{0.8}Li_{0.12}Ni_{0.22}Mn_{0.66}O_2$. The electrochemical performances of the two cathode materials of interest to this study are compared in Fig. 2. We note that electrochemical data are shown here for reference only, and the reader is referred to previous studies by Lu *et al.*,[2] Lee *et al.*,[3] and Xu *et al.*[19] for more detailed accounts of the electrochemical properties of these materials. Rate performance (Fig. 2b) and capacity retention (Fig. 2c) of the unsubstituted material are limited by a P2 to O2 phase transition above 4.2 V (as seen by the plateau in this voltage window), and by various Na^+ ion/vacancy ordering transitions evidenced by voltage steps at 3.5 V and 4.0 V (Fig. 2a).[2,3] Both Mg[16,17] and Li[18,19] substitution for Ni in the honeycomb ordered P2-$Na_{2/3}Ni_{1/3}Mn_{2/3}O_2$ structure (see Fig. 1) lead to a smoother voltage profile (Fig. 2a), no (apparent) structural transformation to the O2 phase (as probed by X-ray diffraction), higher rate performance (Fig. 2b), and improved long-term cyclability (Fig. 2d). Further insight into the composition–structure–property relationship for the Li-substituted phases, to identify the origins of this improved performance, is the purpose of this study.

As a local probe technique, solid-state nuclear magnetic resonance (ssNMR) is ideally suited for the investigation of highly disordered phases formed upon electrochemical cycling of battery materials.[1,20] Here, it is used to monitor variations in the local structure and changes in the oxidation state of the electrochemically-active Ni species.[3,19] Specifically, this work

builds upon our recent study investigating the role of Li doping in the P2-$Na_{0.8}Li_{0.12}Ni_{0.22}Mn_{0.66}O_2$ cathode.[19] In this earlier study, the assignment of ^7Li ssNMR data was based on previous reports on related lithium-containing cathode materials.[20–23] Here we go further, monitoring electronic processes and changes in the Na and Li local environments as a function of charge and discharge in P2-$Na_{2/3}Ni_{1/3}Mn_{2/3}O_2$ and Li-doped P2-$Na_{0.8}Li_{0.12}Ni_{0.22}Mn_{0.66}O_2$, using a combination of ssNMR and first principles NMR calculations.

We find that ssNMR provides insight into Na/Li-ion motion within and between the layers at different stages of (dis)charge and into the high voltage structural processes occurring in P2-$Na_x[Li_yNi_zMn_{1-y-z}]O_2$ compounds. First principles calculations of ^7Li NMR parameters, using the methodology developed in our group,[20,24–26] allow us to refine our previous assignments of P2-$Na_xLi_{0.12}Ni_{0.22}Mn_{0.66}O_2$ spectra.[19] In turn, the comprehensive assignment of the Li data confirms that there are only few TMO_2 layer shifts in the Li-doped compound at high voltage, which are reversible upon electrochemical cycling. Given that very few reports exist on the ^{23}Na NMR of electrochemically-cycled sodium transition metal oxides (none on Ni- and Mn-containing oxides),[11,27] first principles calculations of ^{23}Na NMR parameters are particularly valuable for the interpretation of the experimental data. Although two Na crystallographic environments are present in the P2 layers, a single ^{23}Na NMR signal is observed. The shift of this resonance is in-between those computed for edge- and face-centered prismatic sites in the material, indicating that Na-ion motion between sites in the P2 layers is faster than the NMR timescale and results in an average signal.

Lu and Dahn demonstrated that water intercalation does not take place in as-prepared P2-$Na_{2/3}Ni_{1/3}Mn_{2/3}O_2$;[28] on the other hand several reports have shown that partially desodiated P-type $Na_x TMO_2$ phases ($x \leq 0.35$) become highly hygroscopic.[3,29] Here, low frequency Na and Li signals observed at high voltage are ascribed to local environments formed upon water intercalation in the interlayer space. This interpretation is in contrast with a very recent ^{23}Na NMR study by Yang and coworkers on P2-$Na_{2/3}Ni_{1/3-x}Zn_xMn_{2/3}O_2$ ($x = 0$, 0.07) compounds,[30] as will be further discussed later.

Finally, a comparison of the NMR data obtained for the undoped and Li-doped compounds provides insight into the effect of Li substitution on the high voltage structural processes occurring in P2-$Na_x[Li_yNi_zMn_{1-y-z}]O_2$ cathode materials.
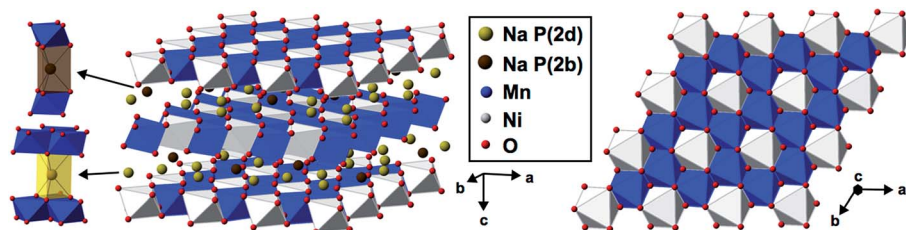

Fig. 1 Side (left) and top (right) view of the ground state P2-$Na_{2/3}Ni_{1/3}Mn_{2/3}O_2$ structure obtained from first principles.[3] Honeycomb ordering of the Ni and Mn cations in the transition metal (TM) layers leads to a $\sqrt{3}a \times \sqrt{3}a$ expansion of the hexagonal $P6_3/mmc$ unit cell (where a is the cell parameter of the material with no cation ordering). Na site occupation reflects the ground state Na^+ ion/vacancy arrangement obtained from DFT+U calculations,[3] resulting in a 1 : 3 occupation ratio of face- to edge-centered prismatic (P(2b) to P(2d), respectively) sites shown on the left.
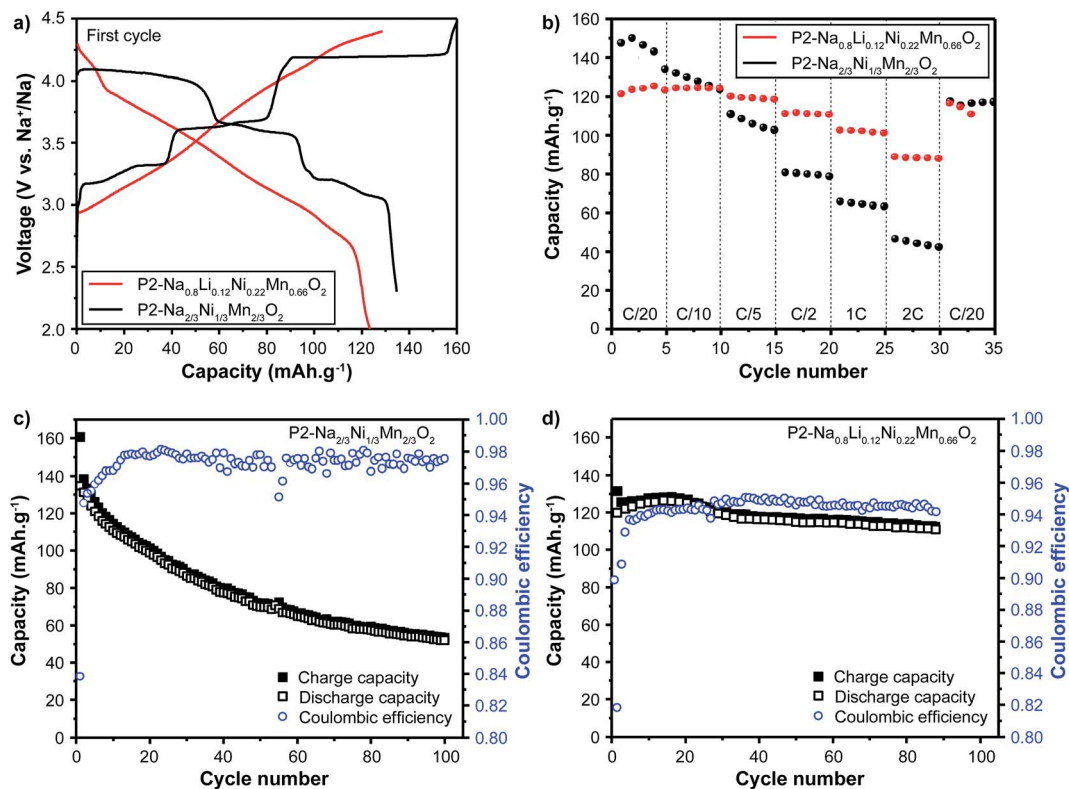
Fig. 2 Comparison of the electrochemical properties of the P2-$Na_{2/3}Ni_{1/3}Mn_{2/3}O_2$ and Li-substituted P2-$Na_{0.8}Li_{0.12}Ni_{0.22}Mn_{0.66}O_2$ cathode materials: (a) electrochemical profiles obtained for the first charge/discharge cycle; (b) rate performance; and long-term cyclability of (c) P2-$Na_{2/3}Ni_{1/3}Mn_{2/3}O_2$ and (d) P2-$Na_{0.8}Li_{0.12}Ni_{0.22}Mn_{0.66}O_2$. In (a) and (c) P2-$Na_{2/3}Ni_{1/3}Mn_{2/3}O_2$ was cycled between 2.3 and 4.5 V *vs.* Na^+/Na at a rate of C/20. In (a) and (d) P2-$Na_{0.8}Li_{0.12}Ni_{0.22}Mn_{0.66}O_2$ was cycled between 2.0 and 4.4 V *vs.* Na^+/Na at a rate of C/10.

2. Experimental and methodology

2.1. Materials preparation

The $Na_{2/3}Ni_{1/3}Mn_{2/3}O_2$ material was synthesized by co-precipitation. Stoichiometric amounts of the precursors, $Mn(NO_3)_2 \cdot 4H_2O$ and $Ni(NO_3)_2 \cdot 6H_2O$, were dissolved in deionized water. The transition metal nitrate solutions were titrated into a stoichiometric NaOH solution using a peristaltic pump at 10 ml h^{-1} rate. The solution was stirred slowly to insure homogeneity. The co-precipitated solid $M(OH)_2$ phase was centrifuged and washed three times with deionized water. The co-precipitated material was dried in the oven to remove excess water and was ground with a stoichiometric amount of Na_2CO_3. The material was precalcined at 500 °C for 5 h and calcined in pellet form at 900 °C for 14 h in a 50 ml porcelain crucible. The synthesis protocol for the P2-$Na_{0.8}Li_{0.12}Ni_{0.22}Mn_{0.66}O_2$ material was described in our previous study.[19]

2.2. Preparation of electrochemically-cycled samples

The slurry was made by mixing 80 wt% of active material (based on the total mass of the P2-$Na_{2/3}Ni_{1/3}Mn_{2/3}O_2$ composite), 10 wt% of polyvinylidene fluoride (PVDF), and 10 wt% acetylene carbon black in *n*-methyl-2-pyrrolidone. The slurry was cast on aluminum foil and dried in a vacuum oven at 80 °C. The electrodes were assembled in 2032 coin cells using GF/F (Whatman) glass fiber filter as the separator, 1 M $NaPF_6$ in propylene carbonate (PC) as electrolyte, and sodium metal was used as the counter electrode. Battery assembly was carried out in an MBraun glovebox (H_2O < 0.1 ppm). Galvanostatic discharge and charge were performed using an Arbin BT2000 battery cycler at C/10 rate. To prepare the electrodes for *ex situ* ssNMR and XRD, the cycled batteries were disassembled in an Ar-filled glovebox. The electrodes were washed with battery grade dimethyl carbonate (DMC) three times and dried at room temperature in the glovebox. The material was stripped off the aluminum current collectors and placed in small vials. The vials were sealed in an aluminum pouch filled with argon (99.9999% pure) to avoid air contamination. The preparation of P2-$Na_xLi_{0.12}$-$Ni_{0.22}Mn_{0.66}O_2$ and electrochemically-desodiated samples was described in our previous study.[19] Briefly, electrodes were prepared by mixing 85 wt% of active material, 5 wt% poly-tetrafluoroethylene (PTFE), and 10 wt% acetylene carbon black. 1 M $NaPF_6$ dissolved in a 2 : 1 mixture of battery grade diethyl carbonate (DEC) and ethylene carbonate (EC) was used as the electrolyte, and sodium metal was used as the counter electrode. The cells were cycled at a rate of C/10.

2.3. *Ex situ* X-ray diffraction (XRD)

The cycled cathode samples were mounted on an XRD sample holder and sealed with polyimide (Kapton) tape. XRD patterns

This journal is © The Royal Society of Chemistry 2017

J. Mater. Chem. A, 2017, 5, 4129–4143 | 4131

were collected at ambient temperature on a Bruker D8 Advance diffractometer, using a LynxEye detector at 40 kV and 40 mA, and a CuKα source ($\lambda = 1.5418$ Å). XRD data were acquired every 0.02° over the 2θ range 10 to 70°. The data collection time for each XRD scan was set to 1 minute. Rietveld refinement[31] of the XRD data was carried out using the FullProf software package.[32]

2.4. Solid-state nuclear magnetic resonance (ssNMR)

^{7}Li, ^{23}Na and ^{1}H ssNMR spectra were acquired at room temperature on a Bruker Avance III 200 wide-bore spectrometer (4.7 T external magnetic field), at Larmor frequencies of −77.9, −53.0 and −200.1 MHz respectively. All NMR experiments were performed using a 1.3 mm double-resonance HX probe. ^{23}Na and ^{7}Li NMR experiments were performed under 60 kHz magic angle spinning (MAS) and using a recycle delay of 30 ms. ^{1}H NMR experiments were performed under 40 kHz MAS and using a 10 ms recycle delay. ^{7}Li, ^{23}Na and ^{1}H NMR chemical shifts were referenced against solid [7]Li$_2$CO$_3$, [23]NaCl and adamantane at 0, 7.21 and 1.87 ppm, respectively. [7]Li spin echo experiments were performed using a 90° RF (radio frequency) pulse of 0.95 μs and a 180° RF pulse of 1.9 μs at 50 W. [7]Li pj-MATPASS experiments[33] were performed using a 90° RF pulse of 0.95 μs at 50 W. ^{23}Na spin echo NMR spectra were acquired using a central transition selective 90° RF pulse of 1.03 μs and a 180° RF pulse of 2.06 μs at 25.04 W. ^{1}H spin echo NMR data were acquired using a 90° RF pulse of 0.75 μs and a 180° RF pulse of 1.5 μs at 64 W. Additional ^{23}Na ssNMR experiments were performed on a Bruker Avance III 700 wide-bore spectrometer (16.44 T external magnetic field), at a Larmor frequency of −185.4 MHz, using a 1.3 mm double-resonance HX probe. ^{23}Na spin echo NMR spectra were acquired on as-synthesized P2-Na$_{2/3}$Ni$_{1/3}$Mn$_{2/3}$O$_2$ and P2-Na$_{0.8}$Li$_{0.12}$Ni$_{0.22}$Mn$_{0.66}$O$_2$ using a 90° RF pulse of 0.55 μs and a 180° RF pulse of 1.1 μs at 100 W, and a recycle delay of 30 ms. Sample temperature was monitored using a variable temperature unit and a fridge connected to the NMR probe and determined from the [207]Pb shift of a Pb(NO$_3$)$_2$ sample. Lineshape analysis was carried out using the SOLA lineshape simulation package within the Bruker Topspin software. Transverse (T'_2) relaxation times were obtained from an exponential fit of the decay of the signal intensity obtained as the echo delay was increased in an NMR spin echo pulse sequence, using an in-house MATLAB code written by Prof. Andrew Pell. The [23]Na spectra presented in this paper are scaled according to the total Na content (x_{Na}) in each sample determined from the observed capacity of the different ex situ cells.

[7]Li and [23]Na, with spin $I = 3/2$, are quadrupolar nuclei. The quadrupolar interaction strength is proportional to the quadrupole moment of the NMR nucleus and the electric field gradient (EFG) at the nucleus. In Na$_x$[Li$_y$Ni$_z$Mn$_{1-y-z}$]O$_2$ compounds, paramagnetic (or hyperfine) interactions take place between the nucleus under observation and unpaired electrons notionally resident on nearby transition metal (TM) species. Through-space hyperfine dipolar coupling is only partially averaged out by fast sample spinning at the magic angle (MAS) and contributes to the intensity of the spinning sidebands. For [7]Li, the quadrupole moment is small and

hyperfine interactions are dominant.[25] The isotropic hyperfine (Fermi contact) shift results from unpaired spin density transfer from the TM d orbitals to the Na nucleus, either directly (through-space) or via an intervening p orbital on O (through-bond). When the magnetic susceptibility tensor is anisotropic, the through-space electron-nuclear dipolar interaction gives rise to a small pseudo-contact shift. Here, the Fermi contact contribution is large and the pseudo-contact term can be neglected.[20] The overall [7]Li shift is approximated to the Fermi contact shift:

$$\delta_{exp}(^7\text{Li}) = \delta_{iso} \tag{1}$$

Quadrupolar interactions are significant for [23]Na and the second-order term leads to a quadrupolar-induced shift (δ_{QIS}). The experimental [23]Na shift (δ_{exp}) is the sum of the field-independent isotropic shift (δ_{iso}) and of the field-dependent δ_{QIS}:

$$\delta_{exp}(^{23}\text{Na}) = \delta_{iso} + \delta_{QIS} \tag{2}$$

In this work, hyperfine and quadrupolar NMR parameters were calculated from first principles in a number of structures, as described below.

2.5. First principles calculations of ^{7}Li and ^{23}Na NMR parameters

Spin-unrestricted hybrid DFT/HF calculations were performed to determine NMR parameters and magnetic coupling strengths in honeycomb ordered Na$_x$Ni$_{1/3}$Mn$_{2/3}$O$_2$ ($x = 2/3$, $1/3$) and Na$_{0.83}$Li$_{0.16}$Ni$_{0.16}$Mn$_{0.67}$O$_2$ structures. The CRYSTAL09 all-electron linear combination of atomic orbital code was used[34,35] and two spin-polarized exchange–correlation functionals based upon the B3LYP form,[36–39] with Fock exchange weights of $F_0 = 20\%$ (H20) and 35% (H35), were applied. Full details of the DFT calculations, including the basis sets and numerical parameters used, are presented in the ESI.†

2.6. Computation of magnetic scaling factors $\Phi(T)$

The method adopted here to compare the NMR parameters obtained from first principles with the experimental NMR data was described in a previous study[25] and is further discussed in the ESI.† Briefly, first principles [7]Li and [23]Na Fermi contact shifts are obtained on ferromagnetic cells (all Ni and Mn spins co-aligned), corresponding to the saturated magnetic moment $M_{sat,i}$. The computed shifts are subsequently scaled to a value consistent with the magnetic state of the system at the temperature of the NMR experiments, using a magnetic scaling factor of the form:

$$\Phi_i(T_{exp}) = \frac{\langle M_i(T_{exp}) \rangle}{M_{sat,i}} \tag{3}$$

where $\langle M_i(T_{exp}) \rangle$ is the temperature-dependent average magnetic moment evaluated at the sample experimental temperature, T_{exp}. T_{exp} is set to 320 K to account for frictional heating introduced by fast rotation of the NMR rotor (60 kHz).

4132 | J. Mater. Chem. A, 2017, 5, 4129–4143

This journal is © The Royal Society of Chemistry 2017

Magnetic moments for the various Ni and Mn site types in honeycomb ordered P2-$Na_xNi_{1/3}Mn_{2/3}O_2$ (x = 2/3, 1/3) and P2-$Na_{0.83}Li_{0.16}Ni_{0.16}Mn_{0.67}O_2$ were determined from simulations using an in-house modification of a Monte Carlo code developed by Harrison and coworkers.[40–42] The code is capable of simulating both cation and magnetic disorder and the underlying theory can be found in Harrison *et al.*'s previous work.[40] The present version of the code will be the subject of a separate publication. The code implements an Ising spin magnetic model with Hamiltonian presented in eqn (S4) in the ESI.† Site-specific scaling factors obtained at 320 K and an external magnetic field of 4.7 T for $Na_xNi_{1/3}Mn_{2/3}O_2$ (x = 2/3, 1/3) and $Na_{0.83}Li_{0.16}Ni_{0.16}Mn_{0.67}O_2$ are presented in Table S3a–c in the ESI.† For comparison, a bulk value was determined from the experimental magnetic susceptibility data obtained for P2-$Na_{2/3}Ni_{1/3}Mn_{2/3}O_2$, as discussed in the ESI.† The field cooled DC magnetic susceptibility data was acquired on a commercial magnetic property measurement system (MPMS) over the temperature range 2 to 350 K and at an external field of 1000 Oe.

3.   Results and discussion

3.1.   Experimental and first principles ^{23}Na NMR study of the model P2-$Na_{2/3}Ni_{1/3}Mn_{2/3}O_2$ cathode material

3.1.1.   *Ex situ* ^{23}Na ssNMR on electrochemically-cycled P2-$Na_{2/3}Ni_{1/3}Mn_{2/3}O_2$. Experimental ^{23}Na ssNMR spectra collected

on different samples along the first electrochemical cycle of P2-$Na_{2/3}Ni_{1/3}Mn_{2/3}O_2$ are presented in Fig. 3.

The overlapping resonances in the spectrum observed upon Na reinsertion at 2.3 V discharge have similar shifts to those observed in the pristine sample, indicating reversibility in the sodiation process. As mentioned in the experimental section, the overall ^{23}Na shift is the sum of a large isotropic hyperfine (paramagnetic) term, the Fermi contact shift, and a smaller second-order quadrupolar contribution (see eqn (2)). The ^{23}Na resonances in the spectra shown above are broad (the full width at half maximum (FWHM) of the resonance observed for as-synthesized P2-$Na_{2/3}Ni_{1/3}Mn_{2/3}O_2$ is approximately 12 kHz) and highly shifted, complicating spectral assignment. The broad NMR lines result from a number of effects: residual broadening due to anisotropic second-order quadrupolar interactions under MAS[20] (most likely minor), anisotropic bulk magnetic susceptibility (ABMS) effects, and frequency overlap between multiple Na resonances, discussed later. In this study, NMR parameters were computed from first principles to help understand the experimental data.

3.1.2. ^{23}Na ssNMR of stoichiometric $Na_{2/3}Ni_{1/3}Mn_{2/3}O_2$

3.1.2.1.   First principles ^{23}Na NMR parameters in $Na_{2/3}Ni_{1/3}Mn_{2/3}O_2$. First principles NMR calculations were performed on honeycomb ordered P2- and O2-$Na_{2/3}Ni_{1/3}Mn_{2/3}O_2$. Na site occupation in the P2 structure, shown in Fig. 1, reflects the
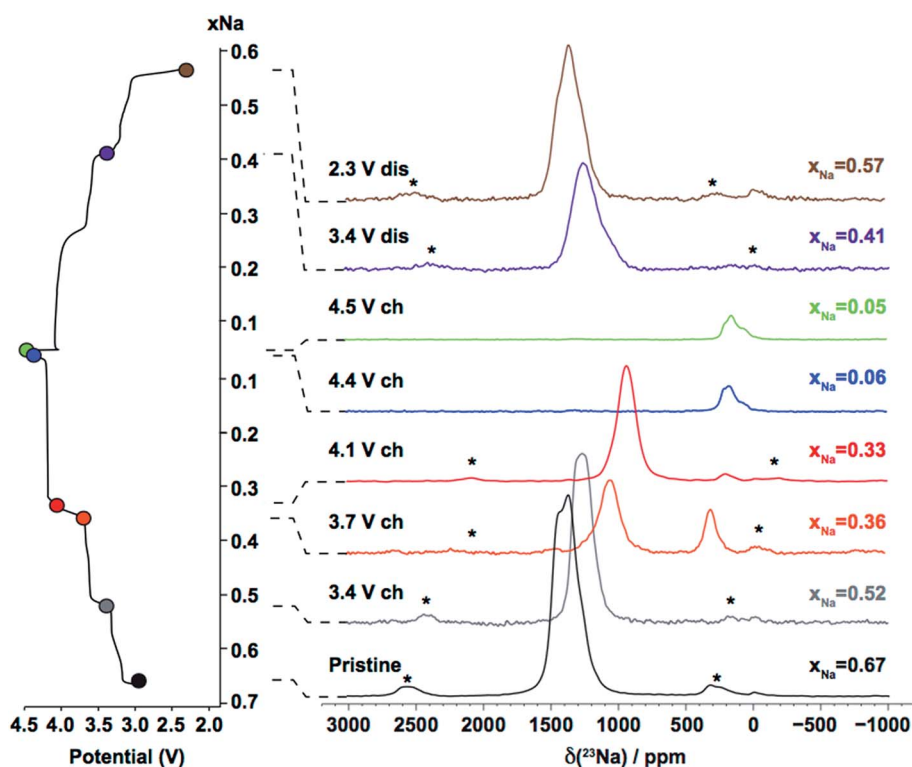

Fig. 3 *Ex situ* ^{23}Na NMR spectra obtained at different stages along the first electrochemical cycle of P2-$Na_{2/3}Ni_{1/3}Mn_{2/3}O_2$. For these and all subsequent NMR spectra, the electrochemical curve is shown on the left hand side, the colored dots indicating the points at which the cells were stopped and the cathode material was extracted for *ex situ* NMR measurements. Spinning sidebands are indicated by an asterisk, the 0 ppm peaks are due to impurity phases containing diamagnetic environments (most likely electrolyte decomposition products or residual Na_2CO_3 starting material). All spectra were collected on samples obtained from a single batch of P2-$Na_{2/3}Ni_{1/3}Mn_{2/3}O_2$, except for the x_{Na} = 0.33 spectrum which was acquired on a sample from a different batch.

ground state Na^+ ion/vacancy arrangement obtained from DFT+U calculations,[3] resulting in a 1 : 3 occupation ratio of face- to edge-centered prismatic (P(2b) to P(2d), respectively) sites. Previous paramagnetic NMR studies have shown that the total Fermi contact shift can be decomposed into individual bond pathway contributions (BPCs) from paramagnetic transition metals in a two-bond coordination shell around the nucleus under observation.[24,26,43,44] The relevant TM–Na interactions, for Na in P(2d) and P(2b) sites, are depicted in Fig. 4a–c. The octahedral (O_h) Na environment present in the O2 structure is shown in Fig. 4d. M and M′ denote metal ions nearest and next nearest to the central Na. The total ^{23}Na Fermi contact shift can be computed as the sum of all M–O–Na and M′–O–Na BPCs. First principles NMR parameters, for the different Na environments depicted in Fig. 4, are presented in Table 1.

Starting with P2-$Na_{2/3}Ni_{1/3}Mn_{2/3}O_2$, the calculated isotropic shifts (δ_{iso}) for type 1 (Fig. 4b) and type 2 (Fig. 4c) P(2b) sites fall between ca. 591 and 932 ppm, while η_Q and C_Q values of 0.1 and 2.9–3.8 MHz, respectively, are obtained. A much larger isotropic shift, in the range 2164–2305 ppm, and η_Q and C_Q values of 0.8 and 5.1 MHz, are computed for the P(2d) site (Fig. 4a). The range of computed shifts is much larger than the linewidth seen experimentally. In O2-$Na_{2/3}Ni_{1/3}Mn_{2/3}O_2$, Na^+ ions in O_h sites are half edge-sharing and half face-sharing with the adjacent metal layers (Fig. 4d), and the isotropic shift, in the range 1401–1589 ppm, is approximately halfway between the shifts of P(2b) and P(2d) Na in the P2 structure.

3.1.2.2. Interpretation of the ^{23}Na ssNMR data collected on the as-synthesized material. In P2-Na_xTMO_2 compounds, both P(2b) and P(2d) sublattices must be occupied in order to minimize in-plane Na^+–Na^+ electrostatic repulsions. P(2b) sites have a larger Na^+–TM^{n+} electrostatic energy penalty and are usually more sparsely populated than P(2d) sites.[3] While various Na local environments are expected with very different hyperfine shifts, NMR studies on this family of materials have consistently reported a single NMR resonance in the ^{23}Na spectrum albeit at a different shift for all the materials that have been studied to date.[11,17,19,30,45,46] Consistent with these earlier reports, the ^{23}Na NMR spectrum of as-synthesized P2-$Na_{2/3}Ni_{1/3}Mn_{2/3}O_2$ acquired at 4.7 T exhibits a single ^{23}Na resonance (see Fig. 3). A spectrum acquired on the same sample at an external magnetic field of 16.44 T is shown in Fig. S1 of the ESI.† The higher magnetic field leads to a greater separation of the resonant frequencies of the different Na sites in the material, and two signals with isotropic shifts of 1511 and 1422 ppm can now be distinguished. These experimental shifts are in-between those computed for P(2b) and P(2d) sites in the structure (see Table 1). As discussed in more detail in the ESI,† the major Na peak in the 16.44 T spectrum is assigned to an average signal due to fast Na^+ ion exchange relative to the NMR timescale between P(2d) and P(2b) sites in the P2 layers. Collapse of the P(2b) and P(2d) NMR signals into a single resonance is indicative of Na^+ ion motion on a timescale that is faster than the largest frequency separation ($\Delta\nu$) between the resonances. Based on the frequency difference between the average P(2b) and P(2d) ^{23}Na NMR shifts computed from first principles, $\Delta\nu \approx 1400$ ppm ≈ 260 kHz at an external field of 16.44 T, Na^+ ion exchange between the different sites occurs at a rate $k > \frac{\pi\Delta\nu}{\sqrt{2}} \approx 578$ kHz.[47] Assuming that long-range Na diffusion results from uncorrelated in-plane Na^+ ion hops between adjacent P(2b) and P(2d) sites, the diffusion coefficient is estimated from the Einstein–Smoluchowski equation:[48] $D_{Na} = \frac{kl^2}{4}$, where l is the minimum distance between 2b and 2d sites, taken as 1.336 Å from the experimental structure determined by Lee et al.[3] We obtain a coefficient $D_{Na} \sim 5 \times 10^{-11}$ cm^2 s^{-1}, lower than the diffusion coefficient determined from a previous GITT measurement,[3] around 2×10^{-9} cm^2 s^{-1}. However, since nearest neighbor P(2b) and P(2d) sites are never simultaneously occupied in P2-type structures, a more appropriate l distance would be the shortest distance between two occupied 2b or 2d sites in the structure (3.336 Å from Lee et al.). Using this number, a diffusion coefficient of 1.6×10^{-10} cm^2 s^{-1} is obtained. Furthermore, we note that the coefficient obtained from the NMR data is a lower bound to the real diffusion coefficient, since we used the minimal value for the exchange rate between the different Na sites that could lead to coalescence of the NMR signals. The low intensity signal at 16.44 T can be fitted with NMR parameters close to those computed for an O_h site in O2-$Na_{2/3}Ni_{1/3}Mn_{2/3}O_2$ (see Table 1) and is therefore assigned to Na in O_h environments in O2-type layers. The integrated intensities of the two signals, scaled by a transverse relaxation factor accounting for the loss of NMR signal intensity over the signal acquisition time (transverse relaxation times of 160 ± 7 μs and 89 ± 13 μs were obtained for the P2 and O2 Na environments, respectively), suggest ca. 10% of Na in O2-type layers. Hence, a small number of O2 stacking faults are present in the majority P2 phase. At 4.7 T, the smaller frequency separation between the
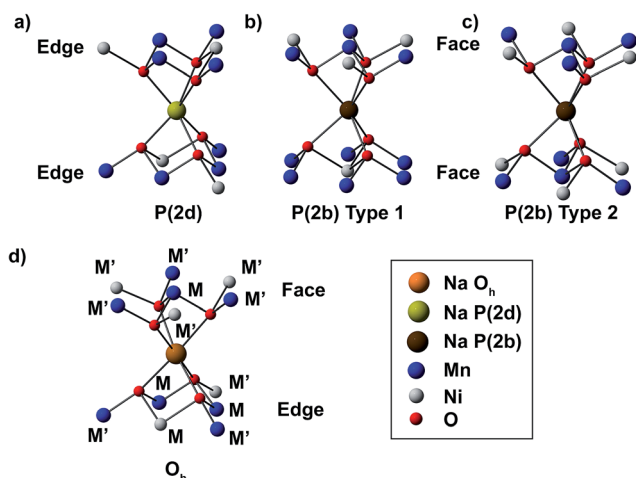

Fig. 4 Na local environments in $Na_{2/3}Ni_{1/3}Mn_{2/3}O_2$. Edge-centered (P(2d)), and type 1 and type 2 face-centered (P(2b)) prismatic sites, present in the ground state P2-$Na_{2/3}Ni_{1/3}Mn_{2/3}O_2$ structure shown in Fig. 1,[3] are shown in (a), (b) and (c), respectively. The octahedral (O_h) Na site in O2-$Na_{2/3}Ni_{1/3}Mn_{2/3}O_2$ is shown in (d). In this and in subsequent diagrams, M and M′ labels indicate metal ions nearest and next nearest to the central atom, respectively.

4134 | J. Mater. Chem. A, 2017, 5, 4129–4143

This journal is © The Royal Society of Chemistry 2017

Table 1 First principles ^{23}Na NMR parameters computed in honeycomb ordered P2- and O2-Na$_{2/3}$Ni$_{1/3}$Mn$_{2/3}$O$_2$ using hybrid HF/DFT and the H20 and H35 functionals. An average Φ scaling factor shown in Table S3a in the ESI, which accounts for residual magnetic couplings between transition metal ions, even in the paramagnetic state, obtained as a weighted average over all metal sites in the P2-Na$_{2/3}$Ni$_{1/3}$Mn$_{2/3}$O$_2$ structure, was used to calculate the overall ^{23}Na hyperfine shifts calculated with both functionals at a sample temperature T of 320 K. P(2b) and P(2d) prismatic sites are present in the P2 structure, and O_h sites in the O2 structure. Type 1 and type 2 P(2b) sites have different Ni/Mn coordination shells. All Na environments are presented in Fig. 4. In this and all subsequent tables the isotropic shift (δ_{iso}, in ppm), dipolar anisotropy ($\Delta_\delta = \delta_{zz} - \frac{1}{2}(\delta_{xx} + \delta_{yy})$, in ppm), dipolar asymmetry (η), quadrupolar coupling constant (C_Q, in MHz), quadrupolar asymmetry (η_Q), second-order quadrupolar shift (δ_{QIS}, in ppm), and net shift ($\delta_{iso} + \delta_{QIS}$, in ppm), are presented for $T = 320$ K and an external magnetic field $B_0 = 4.7$ T

Parameter	Na P(2b)				Na P(2d)		Na O_h	
	Type 1 H20	Type 1 H35	Type 2 H20	Type 2 H35	H20	H35	H20	H35
δ_{iso}/ppm	932	775	861	591	2305	2164	1589	1401
Δ_δ/ppm	1575	1917	1822	2213	1782	2105	1756	2108
η	0.0	0.0	0.0	0.0	0.1	0.1	0.0	0.0
C_Q/MHz	3.2	2.9	3.8	3.5	5.1	5.1	4.4	4.3
η_Q	0.1	0.1	0.1	0.1	0.8	0.8	0.2	0.2
δ_{QIS}/ppm	−92	−76	−126	−111	−291	−289	−175	−164
$\delta_{iso} + \delta_{QIS}$/ppm	840	699	735	480	2013	1875	1414	1237

average P2 Na signal and the resonant frequency of Na$^+$ ions in O2-type layers leads to signal overlap, yielding a single broad peak in the spectrum shown in Fig. 3.

3.1.3. Interpretation of the experimental ^{23}Na ssNMR data ($2/3 \geq x_{Na} \geq 1/3$). Individual Mn^{4+}–O–Na and Ni^{2+}–O–Na bond pathway contributions (BPCs) to the overall ^{23}Na shift were computed in the P2-Na$_{2/3}$Ni$_{1/3}$Mn$_{2/3}$O$_2$ structure using the spin flipping technique developed by Middlemiss et al.[26] The effect of (1) Ni^{2+} to Ni^{3+} oxidation, and (2) structural expansion along the c axis (observed upon initial Na extraction from $x_{Na} = 2/3$ to $1/3$ (ref. 2 and 3)) on the BPCs was investigated in more detail by computing Mn^{4+}–O–Na and Ni^{3+}–O–Na BPCs in the P2-Na$_{1/3}$Ni(III)$_{1/3}$Mn$_{2/3}$O$_2$ structure. The BPCs computed in the P2-Na$_x$Ni$_{1/3}$Mn$_{2/3}$O$_2$ ($x = 2/3, 1/3$) structures are presented in Fig. 5.

The BPCs shown in Fig. 5 are averages over the different values obtained for a given TM–O–Na pathway type due to off-centering of Na$^+$ ions in trigonal prismatic sites in the optimized structure, discussed in more detail in the ESI.† Individual Ni^{3+}–O–A (A = Li$^+$, Na$^+$) BPCs are smaller in magnitude than their Ni^{2+}–O–A (A = Li$^+$, Na$^+$) counterparts, as previously reported in LiNi$_x$Mn$_x$Co$_{1-2x}$O$_2$ materials.[49] In addition, the larger interlayer spacing in the $x = 1/3$ structure generally leads to Mn^{4+}–O–Na BPCs that are smaller in magnitude than those computed in the $x = 2/3$ structure.

The total isotropic shift (δ_{iso}), for a given Na local environment, is obtained by summing the contributions from Mn and Ni ions in M and M′ positions, multiplied by their degeneracies. Total isotropic shifts for the different Na sites in Na$_{2/3}$Ni$_{1/3}$Mn$_{2/3}$O$_2$ and Na$_{1/3}$Ni$_{1/3}$Mn$_{2/3}$O$_2$ are shown in Table 2. The Na$_{2/3}$Ni$_{1/3}$Mn$_{2/3}$O$_2$ reconstructed isotropic shifts in Table 2 are in good agreement with those presented in Table 1 (despite differences in the scaling factors used; see ESI†).

The relative occupation of the different sites in as-synthesized P2-Na$_{2/3}$Ni$_{1/3}$Mn$_{2/3}$O$_2$ can be inferred by comparing the average isotropic P2 shift obtained from a fit

of the experimental data ($\delta_{iso} = 1511$ ppm) to the first principles isotropic shifts computed for P(2b) and P(2d) environments. We note that, given the large ranges of shifts predicted using the H20 and H35 functionals, this method can only yield an approximate occupation ratio. Yet, if the BPCs calculated with the H35 functional (lower shift limit in Table 2) are employed, a 1 : 1.5 occupation ratio of P(2b) : P(2d) sites is determined, in relatively good agreement with the approximately 1 : 1.7 ratio obtained previously from Rietveld refinements of X-ray diffraction (XRD) data on this material.[3]
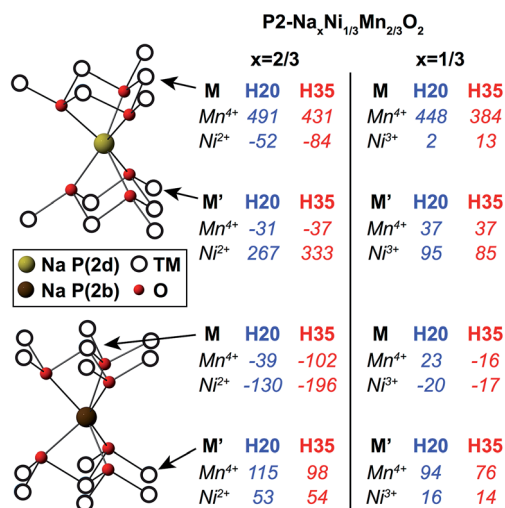

Fig. 5 First principles Mn^{4+}–O–Na and Ni$^{2+/3+}$–O–Na bond pathway contributions (BPCs) to the ^{23}Na Fermi contact shift computed in the optimized P2-Na$_{2/3}$Ni$_{1/3}$Mn$_{2/3}$O$_2$ ($a_{hex} \approx b_{hex} \approx 2.84$ Å, $c = 10.94$ Å) and P2-Na$_{1/3}$Ni$_{1/3}$Mn$_{2/3}$O$_2$ ($a_{hex} \approx b_{hex} \approx 2.83$ Å, $c = 11.53$ Å) structures, using the H20 and H35 functionals. The BPCs determined in P2-Na$_{2/3}$Ni$_{1/3}$Mn$_{2/3}$O$_2$ and P2-Na$_{1/3}$Ni$_{1/3}$Mn$_{2/3}$O$_2$ were scaled using the site-specific scaling factors shown in Table S3a and b in the ESI,† respectively.

This journal is © The Royal Society of Chemistry 2017

J. Mater. Chem. A, 2017, 5, 4129–4143 | 4135

Table 2 Total isotropic shifts (δ_{iso}) for the different Na local environments in $Na_{2/3}Ni_{1/3}Mn_{2/3}O_2$ and $Na_{1/3}Ni_{1/3}Mn_{2/3}O_2$ predicted from the BPCs shown in Fig. 5. The lower and upper shift limits are set by H35 and H20 values, respectively. Of note, O_h Na shifts were also estimated using BPCs computed in $O2\text{-}Na_{2/3}Ni_{1/3}Mn_{2/3}O_2$, yielding a 1305–1556 ppm shift range (HYB35–HYB20) consistent with the range shown above. Site-specific scaling factors Φ were employed, in contrast to the results presented in Table 1, which used an overall scaling factor

	P(2b) type 1	P(2b) type 2	P(2d)	O_h
$Na_{2/3}Ni_{1/3}Mn_{2/3}O_2$	744–1027	705–934	2073–2269	1389–1601
$Na_{1/3}Ni_{1/3}Mn_{2/3}O_2$	696–895	511–705	1881–2134	1196–1420

The most significant result obtained from Table 2 is that a decrease in the total Na isotropic shift is observed upon Ni^{2+} to Ni^{3+} oxidation for all sites in $P2\text{-}Na_xNi_{1/3}Mn_{2/3}O_2$. This is consistent with the experimentally observed decrease in the frequency of the average ^{23}Na NMR peak position observed at the beginning of charge (see Fig. 3), the major Na environment shifting from 1511 ppm ($x_{Na} = 2/3$) to 1030 ppm ($x_{Na} = 1/3$) on charging to 4.1 V. The origin of the 400 ppm peak observed at 3.7 V charge is discussed in the next section. First principles calculations indicate that the main Na peak can be assigned to an average signal due to rapid Na^+ ion motion between sites in the P2 layers (see Tables 1 and 2). Hence, despite the high propensity for Na^+ ion/vacancy ordering at $x_{Na} = 1/2$ and $x_{Na} = 1/3$, as suggested by first principles calculations and by the voltage steps at 3.5 and 4.0 V,[3] Na^+ ion mobility occurs faster than the NMR timescale at least up to 4.1 V at 320 K. This result is consistent with high Na^+ diffusion rates of the order of 7×10^{-9} to 1×10^{-10} cm^2 s^{-1} obtained previously from GITT measurements over the range $2/3 \geq x_{Na} \geq 1/3$.[3] Fits of the major Na resonance in the $x_{Na} = 0.52$, 0.36 and 0.33 spectra yield isotropic shifts at 1370, 1160, and 1030 ppm, respectively, and quadrupolar constants in the range 3.1–3.4 MHz. These parameters suggest that P(2d) and P(2b) sites are approximately equally populated between 3.4 and 4.1 V charge at 320 K, in good agreement with previous XRD data.[3] Comparing with the 1 : 1.5 P(2b) : P(2d) occupation ratio determined for the as-prepared material, the present NMR data indicate that Na is extracted preferentially from edge-centered P(2d) sites at the beginning of charge.

Previous electrochemical and diffraction studies have suggested that the transition between the two Na^+ ion/vacancy orderings at $x_{Na} = 1/3$ and $x_{Na} = 1/2$ occurs via a single-phase process or via a two-phase process involving very similar phases.[2,3] As shown in Fig. S2 in the ESI,† a good fit to the NMR spectrum acquired on the $x_{Na} = 0.41$ sample discharged to 3.4 V can be obtained from a superposition of the major resonances observed at 3.4 and 3.7 V charge (at $x_{Na} = 0.52$ and 0.36, respectively). The material discharged to 3.4 V is presumably composed of a major phase similar to that obtained upon charge to 3.4 V (or of a large number of P2 layers with a Na content close to 0.52), as expected from the electrochemistry, and of a minor phase (or a small number of P2 layers) with a lower Na content. The electrochemical profile shown in Fig. 2a

indicates the presence of two processes over the 3.4–3.7 V range on both charge and discharge, suggesting that the 3.4 V discharge sample is not a simple mixture of the $x_{Na} = 0.52$ and 0.36 phases.

3.1.4. High voltage structural processes revealed by ^{23}Na ssNMR. The long electrochemical plateau starting at ca. 4.1–4.2 V charge (Fig. 2a) has been assigned to a P2 to O2 phase transformation.[2,3] This phase transition results from TMO_2 layer glides driven by an increase in the electrostatic repulsions between adjacent layers upon Na removal. P2 to O2 phase transitions,[2,3,10] the formation of O2-like stacking faults in a major P2 phase,[19] and P2 to OP4 phase transitions[4,11,50] have all been reported in a number of Na_xTMO_2 layered compounds at high voltage. In $P2\text{-}Na_xNi_{1/3}Mn_{2/3}O_2$, Lu and Dahn demonstrated using in situ XRD that the phase transition takes place via a two-phase reaction over the composition range $1/3 \geq x_{Na} \geq 0$.[2] All peaks in the in situ XRD patterns collected at 4.4 and 4.5 V charge could be assigned to a disordered $O2\text{-}Ni_{1/3}Mn_{2/3}O_2$ phase with a small interlayer spacing ($c \approx 8.85$–9 Å),[2,3] as compared with that of the $P2\text{-}Na_{1/3}Ni_{1/3}Mn_{2/3}O_2$ phase ($c \approx 11.35$ Å).[2] More recently, the P2 to O2 transformation was directly observed with atomic level resolution by scanning electron microscopy (STEM), confirming the coexistence of the P2 and O2 phases at the microscale along the high voltage plateau.[16]

^{23}Na NMR confirms the presence of residual Na^+ ions in the end-of-charge samples (see Fig. 3). The isotropic shift of the high voltage NMR signal, at ca. 250 ppm (with a shoulder at ca. 130 ppm), is much lower than the average P2 resonance at 1030 ppm in the $x_{Na} = 1/3$ spectrum. In fact, the BPCs shown in Fig. 5 rule out an assignment of the 250 ppm peak to P(2b) or P(2d) sites in P2 layers, or to O_h sites in O2 layers, when the interlayer spacing c is ≈ 11–11.5 Å. Even if all Ni ions were present as diamagnetic Ni^{4+}, the lowest possible shift, corresponding to that of a P(2b) type 2 environment, would still be of ca. 400 ppm.

Two low frequency Na shifts in the range of 270–350 ppm were observed at 4.7 T for a highly crystalline synthetic sample of triclinic Na birnessite, a layered manganese oxide with approximately 2/3 Mn^{4+} and 1/3 Mn^{3+} ions.[51] The two Na resonances were assigned to different local environments obtained from Mn^{3+}/Mn^{4+} ordering in the MnO_2 layers. The small Na shifts in birnessite, roughly half of those observed in all-Mn^{3+} compounds (e.g. $\alpha\text{-}NaMnO_2$ (ref. 27)) and four times smaller than those of mixed-valence Mn^{3+}/Mn^{4+} materials (e.g. $\alpha\text{-}Na_{2/3}MnO_2$), were ascribed to the large interlayer spacing $c \approx 7$ Å ($c \approx 14$ Å for an equivalent P2 phase), leading to fewer Na–O–Mn interactions and/or longer Mn–O bonds. In the case of Na birnessite, previous reports have shown that water molecules are intercalated.[52–54] The similarity of the Na shifts observed for birnessite and for the partially deintercalated $Na_xNi_{1/3}Mn_{2/3}O_2$ phases suggests that the 250 ppm end-of-charge Na shift in the latter compounds results from the uptake of water within the P2 phase that remains, leading to an expansion of the interlayer space. In fact, a number of recent reports on related Na_xTMO_2 compounds have shown that the intercalation of water in the interlayer space is facilitated by the presence of a large number of Na vacant sites, the water molecules occupying free Na sites and

4136 | J. Mater. Chem. A, 2017, 5, 4129–4143

This journal is © The Royal Society of Chemistry 2017

stabilizing the high repulsion of adjacent oxygen layers *via* the formation of hydrogen bridge bonds.[28,55] An interlayer distance *c* close to 14 Å was determined for the hydrated P2 layers in Na_x-$Ni_{0.22}Co_{0.11}Mn_{0.66}O_2$ ($x_{Na} \leq 0.34$),[55] justifying our comparison of the Na shifts in birnessite and in the end-of-charge hydrated $Na_xNi_{1/3}Mn_{2/3}O_2$ phases.

Here, although electrochemically-cycled samples were handled in an Ar-filled glovebox at all times, it is possible that the NMR rotors were not perfectly airtight, resulting in water intercalation in the interlayer space for the more hygroscopic high voltage phases. In fact, previous *ex situ* diffraction results also indicated the formation of a hydrated phase in this material at high voltage.[3] As shown in Fig. 3, the intensity of the 250 ppm resonance increases between 4.1 and 4.5 V (between $x_{Na} = 1/3$ and 0), suggesting that the $Na_xNi_{1/3}Mn_{2/3}O_2$ material becomes increasingly hygroscopic upon Na extraction. The *ca.* 400 ppm shift observed for the $x_{Na} = 0.36$ sample may also be assigned to Na in hydrated P2 layers, the higher average Ni oxidation state leading to a larger total shift. The higher intensity of the 400 ppm signal at 3.7 V charge, as compared with the 250 ppm signal at 4.1 V charge, either indicates that Na is preferentially deintercalated from the expanded P2 layers over the 3.7–4.1 V potential range, or that water exposure was higher for this sample than for samples with $x_{Na} \leq 1/3$. Lu and Dahn showed that, unlike as-prepared $P2-Na_{2/3}Co_xNi_{1/3-x}Mn_{2/3}O_2$, pristine $P2-Na_{2/3}Ni_{1/3}Mn_{2/3}O_2$ is not prone to hydration.[28] Consistent with this, no low frequency Na signals are observed in the ssNMR spectra collected on the as-synthesized phase and for Na contents $x_{Na} \geq 0.41$.

Zhou *et al.*[56] showed that Li-ion motion on the timescale of µs to ms was a major source of fast transverse (T'_2) NMR relaxation (short relaxation times) in lithium-containing paramagnetic cathodes. We recently demonstrated that ^{23}Na T'_2 relaxation times could probe Na-ion motion in layered $P2-Na_x$-$Mg_{1-y}Mn_yO_2$ compounds.[57] Here, the T'_2 relaxation time (in the ms range) of the low frequency signal assigned to Na in hydrated P2 layers is longer than that of the average signal resulting from water-free P2 layers in $Na_{2/3}Ni_{1/3}Mn_{2/3}O_2$ at intermediate stages of charge ($T'_2 = 100 \pm 8$ µs for $x_{Na} = 0.36$; $T'_2 = 243 \pm 11$ µs for $x_{Na} = 1/3$), which is consistent with more sluggish kinetics of Na^+ ions in the former layer type and suggests that intercalated water molecules hinder fast Na^+ ion diffusion.

In their recent ^{23}Na NMR work on $P2-Na_{2/3}Ni_{1/3-x}Zn_xMn_{2/3}O_2$ ($x = 0, 0.07$) compounds, Yang and co-workers[30] also reported a Na resonance at 230–240 ppm appearing at the end of charge.[30] They speculated that this low frequency peak was indicative of a high voltage phase transformation to a Z phase different from the O2 phase reported to date,[2,3,16] and characterized by the presence of Ni ions in tetrahedral sites in the interlayer space. Yet, the authors did not provide any evidence for Ni migration or the formation of vacancies in the TM layers. The high voltage Z phase was first introduced by Nazar and coworkers, who showed, using X-ray pair distribution analysis, that 12.5% of the TM ions – mainly Fe^{3+} – migrated to tetrahedral sites in the interlayer space upon Na deintercalation from $P2-Na_x[Fe_{1/2}Mn_{1/2}]O_2$.[58] The authors also showed that Ni substitution for Fe effectively

mitigated TM migration at high voltage, with only 3.1% of TM ions observed in tetrahedral interlayer sites in the high voltage $Na_{0.1}Fe_{0.2}Mn_{0.65}Ni_{0.15}O_2$ phase,[58] suggesting that minimal TM migration to the interlayer space should occur upon charge of the $P2-Na_xMn_{2/3}Ni_{1/3}O_2$ cathode. To date, we have not seen any evidence for tetrahedral site occupancy by TM ions, nor the formation of vacancies in the TM layers, in this class of materials,[3,19] suggesting that Yang and coworkers' interpretation of the end-of-charge ^{23}Na NMR data is not valid, at least for our system.

3.2. Experimental and first principles ^{23}Na and ^7Li NMR study of the Li-doped $P2-Na_{0.8}Li_{0.12}Ni_{0.22}Mn_{0.66}O_2$ cathode

As shown in Fig. 2, Li substitution enhances the electrochemical performance of the $P2-Na_{2/3}Ni_{1/3}Mn_{2/3}O_2$ cathode. Previous reports revealed that Li doping prevents transitions between different Na^+ ion/vacancy orderings and delays the high voltage P2 to O2 phase transformation.[18,19,59] Here, we directly compare the local structural changes observed upon cycling for $P2-Na_{0.8}Li_{0.12}Ni_{0.22}Mn_{0.66}O_2$ to those observed for $P2-Na_{2/3}Ni_{1/3}-Mn_{2/3}O_2$ discussed earlier, probing both Na and Li environments with NMR, to gain further insight into the effect of Li substitution on the high voltage structural changes, and to rationalize the higher electrochemical performance of the Li-doped material.

3.2.1. High field ^{23}Na NMR on as-synthesized $P2-Na_{0.8}$-$Li_{0.12}Ni_{0.22}Mn_{0.66}O_2$. A series of spectra collected on as-synthesized $P2-Na_{0.8}Li_{0.12}Ni_{0.22}Mn_{0.66}O_2$ at 16.44 T and at different spinning speeds (and hence different sample temperatures) are shown in Fig. 6.

The NMR signal assigned to the P2 phase (indicated by a red asterisk) is clearly observed at 60 kHz MAS, yet the
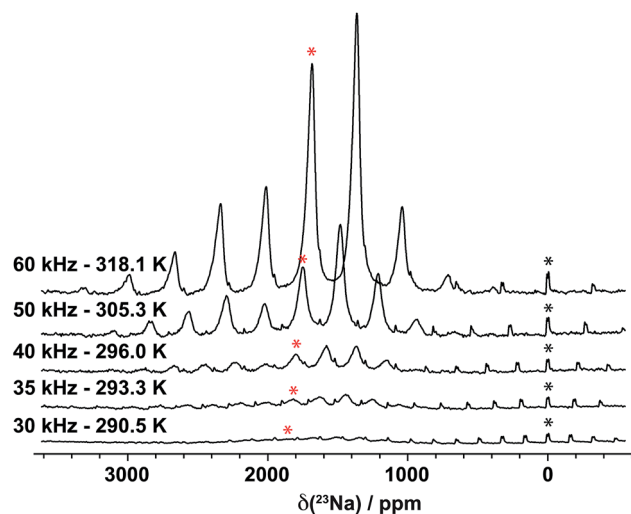

Fig. 6 ^{23}Na NMR spectra collected on as-synthesized $P2-Na_{0.8}$-$Li_{0.12}Ni_{0.22}Mn_{0.66}O_2$ at an external field of 16.44 T. The spectra are scaled according to the number of scans. The data were acquired at various spinning speeds, resulting in different sample temperatures, as indicated. The centerband of the average Na site in the P2 phase, and of the diamagnetic Na_2CO_3 impurity at 0 ppm, are indicated by red and black asterisks, respectively.

linebroadening of the individual peaks within the spinning sideband manifold increases with decreasing spinning speed, from 60 to 30 kHz. Previous NMR studies[60,61] have shown that, in the presence of motion on an appropriate timescale, the MAS technique fails to suppress anisotropic interactions in the spin echo experiment, resulting in significant broadening of the NMR lineshape. The data shown in Fig. 6 suggest that the MAS rate approaches the width of the NMR lines (*i.e.* the size of the anisotropy) as it is reduced from 60 to 30 kHz. At about 30 kHz MAS, Na-ion motion prevents refocusing of the anisotropic (paramagnetic and quadrupolar) interactions, resulting in a very broad, low intensity signal, confirming that the Na^+ ions are mobile in this sample. This result is significant, as, although a few NMR studies on P2-$Na_x TMO_2$ suggested that fast Na^+ ion diffusion in the interlayer space accounts for the unique Na resonance observed in the spectrum,[11,17,19,30,45,46] this is the first time that evidence is obtained for this phenomenon. Here, fast Na^+ ion motion is proven both experimentally, with the gradual broadening of the spectrum shown in Fig. 6, and theoretically, since the unique Na resonances observed experimentally for as-synthesized P2-$Na_x Ni_{1/3} Mn_{2/3} O_2$ (Fig. 3) and P2-$Na_{0.8} Li_{0.12}$-$Ni_{0.22} Mn_{0.66} O_2$ (Fig. 6 and 7) are in-between those computed for P(2b) and P(2d) Na sites (see Table 1). Fast Na^+ ion motion in the 2D planes explains the high rate performance of a number of P2-type $Na_x TMO_2$ cathode materials.[62,63]

3.2.2. *Ex situ* ^{23}Na ssNMR on electrochemically-cycled P2-$Na_{0.8} Li_{0.12} Ni_{0.22} Mn_{0.66} O_2$.

Ex situ ^{23}Na ssNMR spectra recorded at 4.7 T on different samples along the first electrochemical cycle of P2-$Na_x Li_{0.12} Ni_{0.22} Mn_{0.66} O_2$ are presented in Fig. 7. The data enclosed by a black rectangle (in this and in Fig. 8) were

collected on a 4.4 V charged sample ($x_{Na} = 0.35$) obtained from a second P2-$Na_x Li_{0.12} Ni_{0.22} Mn_{0.66} O_2$ batch (sample #2, hereafter), prepared and cycled under similar conditions as the $x_{Na} = 0.35$ sample obtained from the first batch (sample #1). A comparison of two end-of-charge samples is important to correlate changes in the Na and Li local environments at high voltage.

Partial substitution of Ni^{2+} ions by Li^+ in the TM layers results in an increase in the average isotropic shift for Na in the P2 layers, shifting from 1511 ppm in $Na_{2/3} Ni_{1/3} Mn_{2/3} O_2$ (see Fig. 3) to 1647 ppm in $Na_{0.8} Li_{0.12} Ni_{0.22} Mn_{0.66} O_2$ (Fig. 7). We note that P2-$Na_{0.8} Li_{0.12} Ni_{0.22} Mn_{0.66} O_2$ exhibits good structural reversibility after one cycle: the average P2 signal observed in the end-of-discharge Na spectrum is similar to that observed in the pristine spectrum.

The progressive decrease in the average Na resonance upon charge is consistent with Ni oxidation. As discussed earlier for the $Na_{2/3} Ni_{1/3} Mn_{2/3} O_2$ cathode, the 250 ppm end-of-charge Na resonance is indicative of water intercalation within the P2 layers at high voltage. The ^{1}H spectrum collected on sample #2, shown in Fig. S3 in the ESI,† corroborates this hypothesis. The large sideband pattern of the ^{1}H spectrum centered at 0 ppm can be fitted with an anisotropy (Δ_δ) of 1167 ppm and an asymmetry (η) of 0.7, clearly indicating the presence of water in the material. The absence of a paramagnetic shift suggests that the protons are not directly bonded to the TM ions, which is consistent with the water O atoms occupying vacant Na sites in the interlayer space and with the protons forming hydrogen bonds with O atoms in adjacent TMO_2 layers. While the 250 ppm ^{23}Na peak
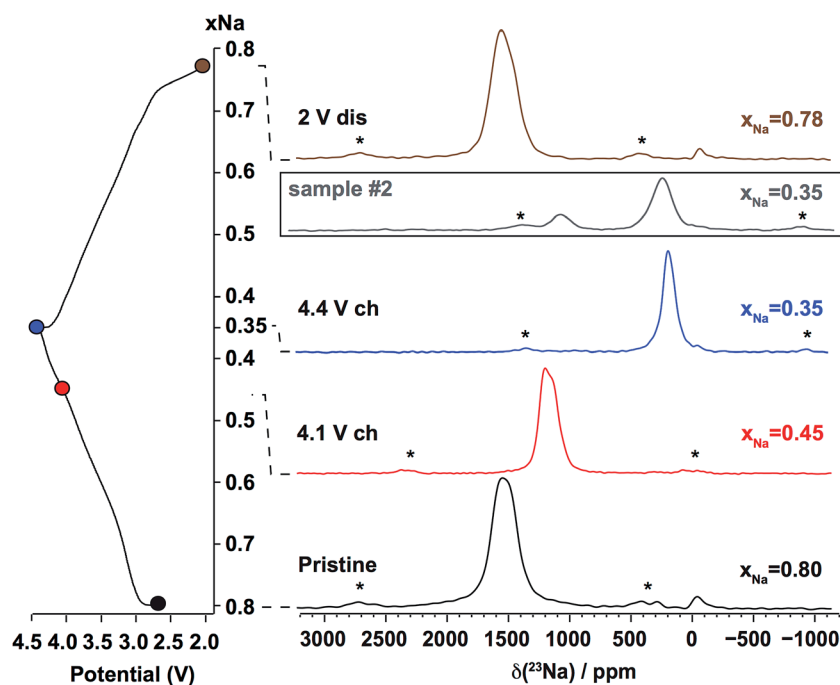

Fig. 7 *Ex situ* ^{23}Na NMR spectra obtained at different stages along the first electrochemical cycle of P2-$Na_{0.8} Li_{0.12} Ni_{0.22} Mn_{0.66} O_2$. The data shown with a solid line were acquired on a first batch of samples. The data enclosed by a black rectangle were obtained for a second sample (sample #2) charged to 4.4 V and are shown for comparison.
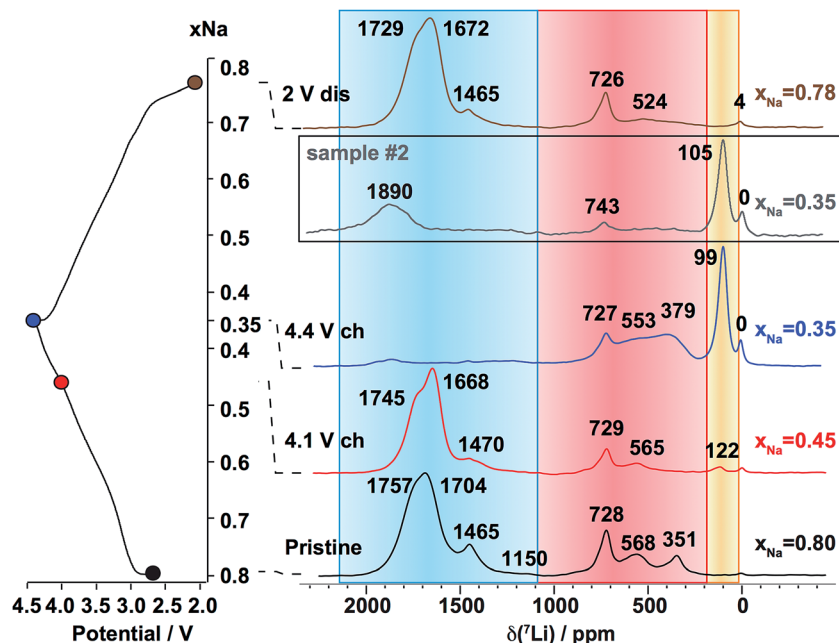
4138 | *J. Mater. Chem. A*, 2017, **5**, 4129–4143

This journal is © The Royal Society of Chemistry 2017

Fig. 8 ^{7}Li pj-MATPASS isotropic NMR spectra obtained at different stages along the first electrochemical cycle of P2-Na$_{0.8}$Li$_{0.12}$Ni$_{0.22}$Mn$_{0.66}$O$_2$. Li shift ranges, for an O_h site in the TM layers (blue), for an O_h site in O2-type Na/Li layers with a large interlayer spacing (red), and for an O_h site in a hydrated O2 layer (yellow), are indicated on the spectra. Spinning sidebands are suppressed in the pj-MATPASS isotropic spectrum[33] and peaks are observed at the resonant frequencies of the different Li environments in the sample. The isotropic shifts are shown on the spectra. The data shown with a solid line were acquired on a first batch of samples and are reproduced here with permission from Xu *et al.*[19] Copyright 2014 American Chemical Society. The data enclosed by a black rectangle were obtained for a second sample charged to 4.4 V (sample #2) and are shown for comparison.

is the only signal observed in the ^{23}Na spectrum collected on sample #1, two peaks are present in the ^{23}Na spectrum collected on sample #2 (see Fig. 7). The low intensity resonance at 1100 ppm in spectrum #2 is consistent with the end-of-charge shift expected for the average Na signal in water-free P2 layers (when the P(2b) : P(2d) site occupation ratio is approximately 1 : 1). The lack of a Na signal at 1100 ppm in spectrum #1 suggests that sample #1 is hydrated to a greater extent than sample #2. Of note, the 250 ppm shift does not depend on the Li/Ni/Mn composition, presumably because the expanded P2 layers result in weak TM–Na interactions and/or because the ordering of the metal ions in the TM layers is close to honeycomb-like and Li$^+$/Ni^{4+} cations have a similar (zero) contribution to the Na shift.

The timescale for water uptake in the 4.4 V charged P2-Na$_x$Li$_{0.12}$Ni$_{0.22}$Mn$_{0.66}$O$_2$ cathode sample was further investigated with *ex situ* XRD. The results, shown in Fig. S4 and discussed in greater detail in the ESI,† reveal that a hydrated P2 phase with an interlayer spacing c comprised between 14.4 and 14.7 Å rapidly forms in the sample, even when air/moisture exposure is minimized. No hydration peaks were observed in the *in situ* synchrotron XRD data presented in our previous study,[19] either suggesting that the *in situ* cell is more airtight than the *ex situ* cell used here (the Kapton tape is expected to be less effective after one day), and/or that the water uptake does not occur quickly enough to be monitored *in situ*. In addition, *in situ* cells have a greater polarization than the coin cells used here to prepare the *ex situ* XRD and NMR samples. Hence, we speculate

that upon charge to 4.4 V, *ex situ* samples have a lower Na content and are more prone to water uptake than *in situ* samples.

3.2.3. *Ex situ* ^{7}Li ssNMR on electrochemically-cycled P2-Na$_{0.8}$Li$_{0.12}$Ni$_{0.22}$Mn$_{0.66}$O$_2$. ^{7}Li NMR spectra obtained at different stages along the first electrochemical cycle of P2-Na$_{0.8}$Li$_{0.12}$Ni$_{0.22}$Mn$_{0.66}$O$_2$ are presented in Fig. 8.

A large number of Li resonances are observed in the spectra shown above. In our previous study,[19] these resonances were assigned to various sites in the TM layers and in the interlayer space by analogy with previous Li NMR studies on related compounds. Here, first principles NMR calculations presented below allow us to make a more detailed assignment of the spectral features.

3.2.4. First principles ^{7}Li NMR parameters in Na$_{0.83}$Li$_{0.16}$Ni$_{0.16}$Mn$_{0.67}$O$_2$ and assignment of the experimental data

3.2.4.1. Li in the TM layers (blue region). In layered materials containing Li$^+$, Ni^{2+}, and Mn^{4+} in the TM layers, Li$^+$ and Ni^{2+} cations have similar ionic radii and occupy metal lattice sites interchangeably. When the (Li + Ni) : Mn ratio is 1 : 2, as in P2-Na$_{0.8}$Li$_{0.12}$Ni$_{0.22}$Mn$_{0.66}$O$_2$, honeycomb ordering is expected. The assignment of the ^{7}Li ssNMR data presented in Fig. 8 is assisted by first principles NMR calculations in a P2-Na$_{0.83}$Li$_{0.16}$Ni$_{0.16}$Mn$_{0.67}$O$_2$ structure featuring a similar honeycomb ordering on the TM lattice as observed in Na$_{2/3}$Ni$_{1/3}$Mn$_{2/3}$O$_2$, save that half of the Ni are replaced by Li (see Fig. S5 in the ESI†). Average values for the first principles Mn^{4+}–O–Li and Ni^{2+}–O–Li BPCs determined for Li in an O_h TM layer site are presented in Fig. 9, while
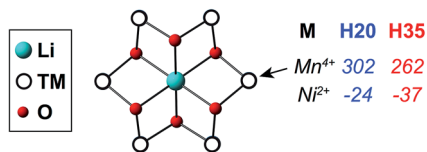
Fig. 9 Average first principles Mn^{4+}–O–Li and Ni^{2+}–O–Li BPCs computed for Li in an O_h TM layer site in P2-$Na_{0.83}Li_{0.16}Ni_{0.16}Mn_{0.67}O_2$ ($a_{hex} \approx b_{hex} \approx 2.88$ Å, $c = 10.83$ Å) using the H20 and H35 functionals. Ni BPCs were computed upon substitution of one Mn by Ni in the first coordination shell around Li. The BPCs were scaled using the Ni and Mn site-specific scaling factors presented in Table S3c in the ESI.†

Fig. 10 First principles Mn^{4+}–O–Li and Ni^{2+}–O–Li BPCs computed for Li in an O_h Na layer site in O2-$Na_{2/3}Ni_{1/3}Mn_{2/3}O_2$ ($a_{hex} \approx b_{hex} \approx 2.89$ Å, $c = 11.05$ Å) using the H20 and H35 functionals. The BPCs were scaled using the scaling factors presented in Table S3a† (Mn scaling factors were averaged).

a full list of the values obtained from individual calculations are shown in Table S4 in the ESI.†

Our previous ^{7}Li NMR study on P2-$Na_{0.8}Li_{0.12}Ni_{0.22}Mn_{0.66}O_2$ demonstrated that Li is preferentially surrounded by Mn^{4+} ions.[19] In this earlier work, Li resonances at *ca.* 1700–1760, 1465 and 1150 ppm were assigned to Li(OMn)$_6$, Li(OMn)$_5$(ONi) and Li(OMn)$_4$(ONi)$_2$ sites in the TM layers. We note that the resonance at *ca.* 1500 ppm can be assigned to either Li(OMn)$_5$(ONi) environments in the pristine phase or to Li(OMn)$_6$ sites in an Li$_2$MnO$_3$ impurity phase.[22,64] On the basis of these assignments, experimental Mn^{4+} and Ni^{2+} BPCs of 290 ± 3 ppm and 18 ± 14 ppm are determined. The experimental Mn^{4+} BPC is consistent with previous studies on Li layered oxide cathodes[20,24] and is intermediate in value between the first principles average BPCs computed using the H20 and H35 functionals shown in Fig. 9. The experimental Ni^{2+} BPC is small and positive, while those obtained from first principles are small and negative. The change in sign may be accounted for by slight differences between the first principles optimized and experimental structures, as discussed in the ESI.†

Although the Mn oxidation state does not change upon electrochemical cycling, a rise in the resonant frequency of the Li(OMn)$_6$ sites, from *ca.* 1700 to 1900 ppm, is observed at the end of charge for sample #2. The Mn^{4+}–O–Li BPCs computed for a range of Li–Mn bond distances and Li–O–Mn bond angles (see Table S4†) show that the higher end-of-charge Li(OMn)$_6$ shift can be accounted for by a decrease in the Mn–Li distance (*i.e.*, a decrease in the *a* lattice parameter[19]) upon Ni oxidation.

3.2.4.2. Li in the Na/Li layers (red region). Li in the interlayer space in layered Li/Ni/Mn oxides typically gives rise to shifts in the 300–800 ppm range shaded in red in Fig. 8.[20–24] The 730 ppm shift observed throughout cycling was previously assigned to an O_h site in the Li layers in a Li$_2$MnO$_3$ impurity phase and the 351 ppm shift observed in the pristine spectrum to a distorted T_d site in a O2/T2 Li$_{2/3}$Ni$_{1/3}$Mn$_{2/3}$O$_2$ (or closely related) impurity phase.[19] A number of additional resonances in the red region of the spectra require further investigation.

While Li$^+$ ions are not usually found in prismatic sites,[65] they can occupy O_h sites *e.g.* in O2 stacking faults in the major P2 phase. Mn^{4+}–O–Li and Ni^{2+}–O–Li BPCs presented in Fig. 10 were computed on an O2-$Na_{2/3}Ni_{1/3}Mn_{2/3}O_2$ supercell in which one Na was substituted by Li, followed by structural relaxation.

Li/Ni/Mn honeycomb ordering in $Na_xLi_{0.12}Ni_{0.22}Mn_{0.66}O_2$ results in a limited number of O_h Li environments in the Na
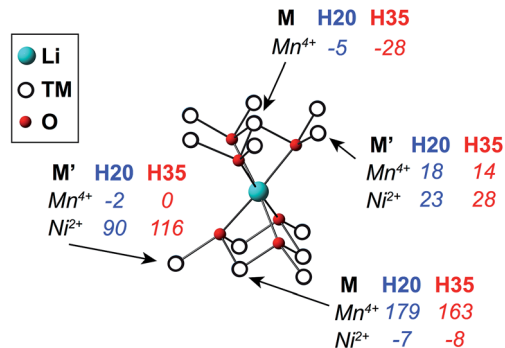
layers. Total isotropic shifts for selected O_h Li environments in a hypothetical O2-$Na_x[Li_yNi_zMn_{1-y-z}]O_2$ structure were computed by summing the Ni and Mn contributions shown above, multiplied by their degeneracies (diamagnetic Li$^+$ ions do not contribute to the Fermi contact shift). The shifts, recorded in Table S5 in the ESI,† lie within the 358–549 ppm range, strongly suggesting that the experimental peak at 568 ppm can be assigned to O_h Li in O2 stacking faults in the as-prepared material; the higher experimental shift is presumably due to slight differences in the TM–O–Li pathway geometries between the experimental and relaxed structures and/or the TM configurations selected for the shift calculations.

An increase in the NMR signal intensity in the red region of the end-of-charge spectrum (see Fig. 8) is indicative of Li migration from the TM layers to the interlayer space, *i.e.* the formation of O2 stacking faults in the major P2 phase.[19] The extent of Li migration is highly sample-dependent, as demonstrated by the very different signal intensities in the red regions of the spectra acquired on the 4.4 V charged samples #1 and #2. Assuming the Ni^{4+} BPCs are zero, end-of-charge Li shifts in the range 339–459 ppm are predicted for the O_h environments considered in Table S5,† which is consistent with the increase in NMR signal intensity at *ca.* 370 ppm for sample #1.

3.2.4.3. Li in hydrated O2 layers (yellow region). The spectra shown in Fig. 7 and 8 reveal that the 250 ppm Na and 100 ppm Li resonances appear at similar stages of cycling, suggesting that the corresponding local environments are structurally related. By analogy with our previous assignment of the high voltage Na data, the low frequency Li shift is assigned to Li in hydrated O2 layers with a larger interlayer spacing.

3.3. What factors affect P2 phase stability at high voltage in $Na_x[Li_yNi_zMn_{1-y-z}]O_2$ cathodes?

Ex situ ^{23}Na and ^{7}Li NMR data collected at different stages of cycling for the undoped $Na_{2/3}Ni_{1/3}Mn_{2/3}O_2$ and Li-doped $Na_{0.8}Li_{0.12}Ni_{0.22}Mn_{0.66}O_2$ cathodes have led to a better understanding of the requirements for good P2 phase stability upon Na deintercalation from $Na_x[Li_yNi_zMn_{1-y-z}]O_2$ cathodes. Our findings are summarized below.

4140 | *J. Mater. Chem. A*, 2017, 5, 4129–4143

This journal is © The Royal Society of Chemistry 2017

As discussed in our previous work,[19] unlike in the undoped P2-$Na_{2/3}Ni_{1/3}Mn_{2/3}O_2$ cathode, ^{7}Li ssNMR shows no evidence for TMO_2 layer glides in P2-$Na_xLi_{0.12}Ni_{0.22}Mn_{0.66}O_2$ below 4.4 V, clearly indicating that Li substitution leads to an extension towards higher voltage of the potential range over which the P2 phase is stable in $Na_x[Li_yNi_zMn_{1-y-z}]O_2$ cathode materials. ^{7}Li ssNMR also reveals reversible Li migration from the TM layers to the interlayer space at high voltage in the P2-$Na_xLi_{0.12}Ni_{0.22}$-$Mn_{0.66}O_2$ cathode. The additional Li NMR data shown in the present work and obtained on different $Na_xLi_{0.12}Ni_{0.22}Mn_{0.66}O_2$ samples charged to 4.4 V (samples #1 and #2) demonstrates that the relative population of TM and Na layer sites by Li at high voltage is sample-dependent: while all Li^+ ions migrate to the Na layers for sample #1, some Li is left in the TM layers for sample #2. Moreover, the combined Li and Na NMR data presented here suggest that the extent of Li migration at the end of charge is correlated with the proportion of Na^+ and Li^+ ions in low frequency environments (resonating at 250 and 100 ppm, respectively), assigned to Na and Li sites formed upon water intercalation in the interlayer space of both P2 and O2 layers. ^{23}Na ssNMR reveals that Li substitution, which leads to a greater number of Na^+ ions remaining in the interlayer space at 4.4 V ($x_{Na} \approx 0.35$ for $Na_xLi_{0.12}Ni_{0.22}Mn_{0.66}O_2$, *vs.* $x_{Na} \approx 0.06$ for $Na_xNi_{1/3}Mn_{2/3}O_2$), delays the (*ex situ*) uptake of water molecules within the P2 interlayer space upon charge, for samples that have been exposed (often unintentionally) to moisture. The characteristic low frequency Na resonance at 250 ppm is observed from 3.7 V for $Na_xNi_{1/3}Mn_{2/3}O_2$, while there is no evidence for hydration before 4.4 V charge for the Li-doped compound (neither in the P2 layers, as revealed by the Na NMR data, nor in O2-type stacking faults, as evidenced by the Li data). It is important to note that, although water molecules are found to intercalate into the layers of partially-deintercalated *ex situ* cathode samples, water intercalation is unlikely to happen during continuous cycling of the electrochemical cells. High structural reversibility and high Na^+ mobility throughout the charge/discharge cycle account for the overall excellent electrochemical performance for the P2-$Na_{0.8}Li_{0.12}Ni_{0.22}Mn_{0.66}O_2$ cathode (see Fig. 2).

Overall, the data presented in this study demonstrate that a large number of vacant sites in P2-type layers favor both O2 stacking fault formation and water intercalation in the interlayer space. The different results obtained for the two end-of-charge $Na_xLi_{0.12}Ni_{0.22}Mn_{0.66}O_2$ samples considered here may also be due to a slightly lower final Na content in sample #1, as compared with sample #2, or to slightly different sample preparation processes or waiting times before the NMR measurements.

4. Conclusions

A comprehensive *ex situ* ssNMR and XRD study of the structural processes occurring upon electrochemical cycling in P2-Na_x-$[Li_yNi_zMn_{1-y-z}]O_2$ ($0 \leq x, y, z \leq 1$) cathode materials was undertaken. The complex assignment of the paramagnetic ^{23}Na and ^{7}Li NMR data was assisted by hybrid HF/DFT calculations of the NMR parameters, the computations providing detailed

insight into the ^{23}Na and ^{7}Li NMR shift mechanisms at all stages of cycling. It is important to note that the first principles ^{23}Na and ^{7}Li NMR parameters presented in this study are transferable and may be used to interpret NMR data obtained on similar P2/O3-Na_xTMO_2 (TM = Ni^{2+}, Ni^{3+}, Ni^{4+}, Mn^{4+}) compounds.

In the present study, we found that fast Na-ion motion in the P2 layers results in an average ^{23}Na NMR signal with a resonant frequency in-between those computed *ab initio* for edge- and face-centered prismatic sites in P2-$Na_x[Li_yNi_zMn_{1-y-z}]O_2$ compounds. This is the first time that experimental and theoretical evidence are provided for fast Na-ion motion (on the NMR timescale) in the interlayer space in P2-type Na_xTMO_2 materials.

In the $Na_xNi_{1/3}Mn_{2/3}O_2$ cathode material, TMO_2 layer glides lead to a complete P2 to O2 phase transition upon Na deintercalation.[2,3] In our previous work,[19] we showed that Li doping delays the P2 to O2 phase transformation to higher voltage, so that local O2 stacking faults are formed in the partially deintercalated P2-$Na_xLi_{0.12}Ni_{0.22}Mn_{0.66}O_2$ compound at 4.4 V. Li migration from the TM layers to O2-type Na layers between 4.1 and 4.4 V was directly observed with ^{7}Li ssNMR. In the present work we showed that, in addition to layer shearing, a large number of Na vacant sites in the interlayer space result in highly hygroscopic end-of-charge phases. The interlayer spacing c of the hydrated P2 and O2 layers was found to be >14 Å (as compared with $c \approx$ 11–11.5 Å for water-free layers), leading to characteristic low frequency Na and Li shifts at the end of charge. Water intercalation into *ex situ* cathode samples was observed from 3.7 V charge ($x_{Na} = 0.36$) for the $Na_xNi_{1/3}Mn_{2/3}O_2$ material, while there was no evidence for water uptake in Na_x-$Li_{0.12}Ni_{0.22}Mn_{0.66}O_2$ samples extracted below 4.4 V charge. It is speculated that the stability of the initial P2 phase, hence the number of O2 stacking faults and extent of water uptake, is intimately linked to the final Na content in the interlayer space upon charge. Li doping results in more Na remaining in the interlayer space upon charge and delays both TMO_2 layer glides and water uptake. Practically speaking, water intercalation is unlikely to happen during continuous cycling of the electrochemical cells, and the high structural reversibility and high Na^+ mobility throughout the charge/discharge cycle account for the overall excellent electrochemical performance for the P2-$Na_{0.8}Li_{0.12}Ni_{0.22}Mn_{0.66}O_2$ cathode.

Acknowledgements

This journal is © The Royal Society of Chemistry 2017

J. Mater. Chem. A, 2017, **5**, 4129–4143 | **4141**

References

1 R. J. Clément, P. G. Bruce and C. P. Grey, *J. Electrochem. Soc.*, 2015, **162**, A2589–A2604.

2 Z. Lu and J. R. Dahn, *J. Electrochem. Soc.*, 2001, **148**, A1225–A1229.

3 D. H. Lee, J. Xu and Y. S. Meng, *Phys. Chem. Chem. Phys.*, 2013, **15**, 3304.

4 N. Yabuuchi, M. Kajiyama, J. Iwatate, H. Nishikawa, S. Hitomi, R. Okuyama, R. Usui, Y. Yamada and S. Komaba, *Nat. Mater.*, 2012, **11**, 512–517.

5 Y.-E. Zhu, X. Qi, X. Chen, X. Zhou, X. Zhang, J. Wei, Y. Hu and Z. Zhou, *J. Mater. Chem. A*, 2016, **4**, 11103–11109.

6 X. Chen, X. Zhou, M. Hu, J. Liang, D. Wu and J. Wei, *J. Mater. Chem. A*, 2015, **3**, 20708–20714.

7 H. Kim, H. Kim, Z. Ding, M. H. Lee, K. Lim, G. Yoon and K. Kang, *Adv. Energy Mater.*, 2016, **6**, 1600943.

8 Y. Li, Z. Yang, S. Xu, L. Mu, L. Gu, Y.-S. Hu, H. Li and L. Chen, *Adv. Sci.*, 2015, **2**, 1500031.

9 C. Delmas, C. Fouassier and P. Hagenmuller, *Physica B+C*, 1980, **99**, 81–85.

10 N. Yabuuchi, R. Hara, K. Kubota, J. Paulsen, S. Kumakura and S. Komaba, *J. Mater. Chem. A*, 2014, **2**, 16851–16855.

11 G. Singh, J. M. L. del Amo, M. Galceran, S. Pérez-Villar and T. Rojo, *J. Mater. Chem. A*, 2015, **3**, 6954–6961.

12 S. Komaba, N. Yabuuchi, T. Nakayama, A. Ogata, T. Ishikawa and I. Nakai, *Inorg. Chem.*, 2012, **51**, 6211–6220.

13 J. Ma, S.-H. Bo, L. Wu, Y. Zhu, C. P. Grey and P. G. Khalifah, *Chem. Mater.*, 2015, **27**, 2387–2399.

14 X. Li, D. Wu, Y.-N. Zhou, L. Liu, X.-Q. Yang and G. Ceder, *Electrochem. Commun.*, 2014, **49**, 51–54.

15 S.-M. Oh, S.-T. Myung, J.-Y. Hwang, B. Scrosati, K. Amine and Y.-K. Sun, *Chem. Mater.*, 2014, **26**, 6165–6171.

16 P. F. Wang, Y. You, Y.-X. Yin, Y. S. Wang, L.-J. Wan, L. Gu and Y.-G. Guo, *Angew. Chem.*, 2016, **128**, 7571–7575.

17 G. Singh, N. Tapia-Ruiz, J. M. Lopez del Amo, U. Maitra, J. W. Somerville, A. R. Armstrong, J. Martinez de Ilarduya, T. Rojo and P. G. Bruce, *Chem. Mater.*, 2016, **28**, 5087–5094.

18 D. Kim, S.-H. Kang, M. Slater, S. Rood, J. T. Vaughey, N. Karan, M. Balasubramanian and C. S. Johnson, *Adv. Energy Mater.*, 2011, **1**, 333–336.

19 J. Xu, D. H. Lee, R. J. Clément, X. Yu, M. Leskes, A. J. Pell, G. Pintacuda, X.-Q. Yang, C. P. Grey and Y. S. Meng, *Chem. Mater.*, 2014, **26**, 1260–1269.

20 C. P. Grey and N. Dupré, *Chem. Rev.*, 2004, **104**, 4493–4512.

21 C. P. Grey, W.-S. Yoon, J. Reed and G. Ceder, *Electrochem. Solid-State Lett.*, 2004, **7**, A290–A293.

22 W.-S. Yoon, S. Iannopollo, C. P. Grey, D. Carlier, J. Gorman, J. Reed and G. Ceder, *Electrochem. Solid-State Lett.*, 2004, **7**, A167–A171.

23 J. Cabana, N. A. Chernova, J. Xiao, M. Roppolo, K. A. Aldi, M. S. Whittingham and C. P. Grey, *Inorg. Chem.*, 2013, **52**, 8540–8550.

24 C. P. Grey and Y. J. Lee, *Solid State Sci.*, 2003, **5**, 883–894.

25 J. Kim, D. S. Middlemiss, N. A. Chernova, B. Y. X. Zhu, C. Masquelier and C. P. Grey, *J. Am. Chem. Soc.*, 2010, **132**, 16825–16840.

26 D. S. Middlemiss, A. J. Ilott, R. J. Clément, F. C. Strobridge and C. P. Grey, *Chem. Mater.*, 2013, **25**, 1723–1734.

27 J. Billaud, R. J. Clément, A. R. Armstrong, J. Canales-Vázquez, P. Rozier, C. P. Grey and P. G. Bruce, *J. Am. Chem. Soc.*, 2014, **136**, 17243–17248.

28 Z. Lu and J. R. Dahn, *Chem. Mater.*, 2001, **13**, 1252–1257.

29 A. Caballero, L. Hernán, J. Morales, L. Sánchez, J. S. Peña and M. A. G. Aranda, *J. Mater. Chem.*, 2002, **12**, 1142–1147.

30 X. Wu, G.-L. Xu, G. Zhong, Z. Gong, M. J. McDonald, S. Zheng, R. Fu, Z. Chen, K. Amine and Y. Yang, *ACS Appl. Mater. Interfaces*, 2016, **8**, 22227–22237.

31 H. M. Rietveld, *J. Appl. Crystallogr.*, 1969, **2**, 65–71.

32 J. Rodríguez-Carvajal, *Abstracts of the Satellite Meeting on Powder Diffraction of the XV Congress of the IUCr*, Toulouse, France, 1990.

33 I. Hung, L. Zhou, F. Pourpoint, C. P. Grey and Z. Gan, *J. Am. Chem. Soc.*, 2012, **134**, 1898–1901.

34 R. Dovesi, R. Orlando, B. Civalleri, C. Roetti, V. R. Saunders and C. M. Zicovich-Wilson, *Z. Kristallogr.*, 2005, **220**, 571–573.

35 R. Dovesi, V. R. Saunders, C. Roetti, R. Orlando, C. M. Zicovich-Wilson, B. Civalleri, F. Pascale, K. Doll, N. M. Harrison, I. J. Bush, P. DArco and M. Llunell, *Crystal09 user's manual*, University of Torino, Torino, Italy, 2010.

36 A. D. Becke, *J. Chem. Phys.*, 1993, **98**, 5648–5652.

37 C. Lee, W. Yang and R. Parr, *Phys. Rev. B: Condens. Matter Mater. Phys.*, 1988, **37**, 785–789.

38 S. H. Vosko, L. Wilk and M. Nusair, *Can. J. Phys.*, 1980, **58**, 1200–1211.

39 P. J. Stephens, F. J. Devlin, C. F. Chabalowski and M. J. Frisch, *J. Phys. Chem.*, 1994, **98**, 11623–11627.

40 R. J. Harrison, *Am. Mineral.*, 2006, **91**, 1006–1024.

41 R. J. Harrison, *Geochem., Geophys., Geosyst.*, 2009, **10**, 1–17.

42 H. S. Nabi, R. J. Harrison and R. Pentcheva, *Phys. Rev. B: Condens. Matter Mater. Phys.*, 2010, **81**, 214432.

43 R. J. Clément, A. J. Pell, D. S. Middlemiss, F. C. Strobridge, J. K. Miller, M. S. Whittingham, L. Emsley, C. P. Grey and G. Pintacuda, *J. Am. Chem. Soc.*, 2012, **134**, 17178–17185.

44 F. C. Strobridge, D. S. Middlemiss, A. J. Pell, M. Leskes, R. J. Clément, F. Pourpoint, Z. Lu, J. V. Hanna, G. Pintacuda, L. Emsley, A. Samoson and C. P. Grey, *J. Mater. Chem. A*, 2014, **2**, 11948.

45 D. Carlier, M. Blangero, M. Ménétrier, M. Pollet, J.-P. Doumerc and C. Delmas, *Inorg. Chem.*, 2009, **48**, 7018–7025.

46 E. Gonzalo, M. H. Han, J. M. L. del Amo, B. Acebedo, M. Casas-Cabanas and T. Rojo, *J. Mater. Chem. A*, 2014, **2**, 18523–18530.

47 M. H. Levitt, *Spin Dynamics: Basics of Nuclear Magnetic Resonance*, John Wiley & Sons, 2nd edn, 2008.

48 P. Heitjans and S. Indris, *J. Phys.: Condens. Matter*, 2003, **15**, R1257–R1289.

49 D. Zeng, J. Cabana, J. Breger, W.-S. Yoon and C. P. Grey, *Chem. Mater.*, 2007, **19**, 6277–6289.

50 J. Billaud, G. Singh, A. R. Armstrong, E. Gonzalo, V. Roddatis, M. Armand, T. Rojo and P. G. Bruce, *Energy Environ. Sci.*, 2014, **7**, 1387–1391.

51 K. A. Aldi, J. Cabana, P. J. Sideris and C. P. Grey, *Am. Mineral.*, 2012, **97**, 883–889.

52 C. L. Lopano, P. J. Heaney, J. E. Post, J. Hanson and S. Komarneni, *Am. Mineral.*, 2007, **92**, 380–387.

53 J. E. Post, P. J. Heaney and J. Hanson, *Powder Diffr.*, 2002, **17**, 218–221.

54 B. Lanson, V. A. Drits, Q. Feng and A. Manceau, *Am. Mineral.*, 2002, **87**, 1662–1671.

55 D. Buchholz, L. G. Chagas, C. Vaalma, L. Wu and S. Passerini, *J. Mater. Chem. A*, 2014, **2**, 13415.

56 L. Zhou, M. Leskes, T. Liu and C. P. Grey, *Angew. Chem., Int. Ed.*, 2015, **54**, 14782–14786.

57 R. J. Clément, J. Billaud, A. R. Armstrong, G. Singh, T. Rojo, P. G. Bruce and C. P. Grey, *Energy Environ. Sci.*, 2016, **9**, 3240–3251.

58 E. Talaie, V. Duffort, H. L. Smith, B. Fultz and L. F. Nazar, *Energy Environ. Sci.*, 2015, **8**, 2512–2523.

59 N. Karan, M. D. Slater, F. Dogan, D. Kim, C. S. Johnson and M. Balasubramanian, *J. Electrochem. Soc.*, 2014, **161**, A1107–A1115.

60 M. M. Maricq and J. S. Waugh, *J. Chem. Phys.*, 1979, **70**, 3300–3316.

61 M. J. Thrippleton, M. Cutajar and S. Wimperis, *Chem. Phys. Lett.*, 2008, **452**, 233–238.

62 Y. Mo, S. P. Ong and G. Ceder, *Chem. Mater.*, 2014, **26**, 5208–5214.

63 L. Liu, X. Li, S.-H. Bo, Y. Wang, H. Chen, N. Twu, D. Wu and G. Ceder, *Adv. Energy Mater.*, 2015, **5**, 1500944.

64 J. Breger, M. Jiang, N. Dupré, Y. S. Meng, Y. Shao-Horn, G. Ceder and C. P. Grey, *J. Solid State Chem.*, 2005, **178**, 2575–2585.

65 S.-W. Kim, D.-H. Seo, X. Ma, G. Ceder and K. Kang, *Adv. Energy Mater.*, 2012, **2**, 710–721.

This journal is © The Royal Society of Chemistry 2017

J. Mater. Chem. A, 2017, **5**, 4129–4143 | **4143**